Materials Advances

ROYAL SOCIETY OF CHEMISTRY

PAPER

View Article Online
View Journal

Cite this: DOI: 10.1039/d6ma00476h

Green route synthesis of cobalt oxide nanoparticles with enhanced electrocatalytic performance for atrazine detection

Simranjeet Singh, †[a] Pavithra N.,†[a] Radhika Varshney,†[a] Praveen C. Ramamurthy, *[a] Joginder Singh [b] and Nabila Shehata [c]

Developing sustainable strategies for monitoring pesticide contamination is vital to protect water quality and human health. In the present work, cobalt oxide nanoparticles were synthesized *via* a green route using the aqueous leaf extract of *Bauhinia purpurea L.* as a bio-reducing agent. A series of analytical techniques, including XRD, TGA, SEM, UV–Vis, XPS, and FTIR, was employed to verify the structural, morphological, optical, and surface chemical characteristics of the nanoparticles. The resulting Cobalt oxide nanoparticles exhibited strong electrocatalytic behavior and were utilized for the electrochemical determination of atrazine. Computational docking studies supported experimental observations by indicating stable interactions between atrazine molecules and the cobalt oxide surface, predominantly through hydrogen bonding. The fabricated sensor demonstrated a linear response from 20–200 μM with a detection limit of 11.8 μM and good selectivity toward atrazine. Application to distilled and wastewater samples demonstrated satisfactory recovery, confirming its practical utility. The study highlights an environmentally benign approach for nanoparticle fabrication and presents an effective platform for rapid atrazine monitoring in aqueous environments.

Received 6th April 2026,
Accepted 22nd May 2026

DOI: 10.1039/d6ma00476h

rsc.li/materials-advances

1. Introduction

In modern agriculture, pesticides are widely applied to maximize production and improve crop quality.[1] However, their excessive use has emerged as a major environmental concern. Overuse of these chemicals has contributed significantly to contamination of soil, water, and food.[2–4] Pesticide exposure is responsible for nearly 0.3 million deaths annually, with millions more suffering from various forms of pesticide-related poisoning.[5] Beyond its impact on human health, pesticide contamination also harms wildlife, aquatic organisms, and the surrounding environment, ultimately disrupting the balance of entire ecosystems.[6,7] To support sustainable agricultural practices and responsibly regulate pesticide application, there is an urgent need for affordable, user-friendly detection technologies to minimize ecological and health risks. Atrazine, a triazine-based herbicide with a molecular mass of 215.68 g mol^{-1}, is among the most frequently applied agrochemicals for weed management in food-crop cultivation.[8] Its extensive agricultural use has given rise to widespread contamination of soil and water systems. Owing to its relatively low aqueous solubility (around 33 mg L^{-1}), atrazine persists for long durations, particularly in aquatic environments, where its degradation is considerably slower than in soil. Continuous exposure to contaminated water has been linked to several health concerns, including endocrine system disruption, hormonal imbalances, heightened risk of breast and prostate cancers, and damage to vital organs, with children being especially vulnerable.[9–12] The World Health Organization recommends a permissible concentration of 2 μg L^{-1} for atrazine in drinking water,[13] with an upper acceptable limit of 3 μg L^{-1}. Considering these risks, developing highly selective and sensitive analytical tools for detecting atrazine in environmental and food samples is crucial for monitoring contamination and ensuring public safety.

Several analytical methods, including enzyme-linked immunosorbent assay (ELISA), fluorescence-based assays, gas chromatography–mass spectrometry (GC–MS), liquid chromatography mass spectrometry (LC–MS), and high-performance liquid chromatography (HPLC), are commonly employed for pesticide detection.[14] Although these conventional techniques offer high sensitivity, reliability, and trace-level analysis, they nevertheless involve costly, sophisticated instrumentation, extensive sample preparation, long processing times, and the

[a] *Interdisciplinary Centre for Water Research (ICWaR), Indian Institute of Science, Bengaluru, Karnataka 560012, India. E-mail: praveen@iisc.ac.in*
[b] *Department of Botany, Nagaland University, HQRS: Lumami, Nagaland 798627, India*
[c] *Environmental Science and Industrial Development Department, Faculty of Postgraduate Studies for Advanced Sciences, Beni-Suef University, Beni Suef, Egypt*
† Equal contribution.

need for trained personnel. Moreover, their suitability for on-site or rapid monitoring, particularly during urgent field assessments, remains limited. Therefore, the development of a sustainable, economical, and user-friendly sensing strategy that can adapt to diverse agricultural scenarios is of great importance. Recently, attention has shifted toward electrochemical sensing techniques, such as amperometric, voltammetric, and impedimetric methods, for the monitoring of atrazine. These platforms are gaining prominence because they provide rapid analysis, low detection limits, high sensitivity, and the capability for real-time, *in situ* measurements. Furthermore, electrochemical sensors are typically portable, economical, and relatively easy to operate, making them promising tools for field-based detection. Although, there are different electrochemical atrazine sensors; however, each sensor has its merits and limitations. For example, Immunosensors is highly selective; LOD down to 0.016 ng mL^{-1} and 0.018 ng mL^{-1} in some formats),[15,16] Aptasensors (Label-free; signal-off mode *via* electron-transfer hindrance; LOD 0.1 pM),[17] Enzymatic biosensors (Inhibition- or catalysis-linked responses; LOD 1.6 μM (HRP-LIGE),[18] 5.4 μM (Ha006a)),[19] Molecularly Imprinted Polymer Sensors (Very high selectivity; LOD as low as 1.5×10^{-13} M and 10 fM),[20] Nanomaterial-enhanced non-enzymatic sensors (Ultra-high sensitivity; many reach pM–zM LOD range),[21] Photoelectrochemical sensors (Rapid photocurrent response; LOD 0.008 μM),[22] Portable/EIS platforms (On-site detection; LOD fg mL^{-1} range).[23] Compared to the above-mentioned electrochemical sensors, the NPs have strong sustainability advantage where plant-extract mediated synthesis reveals low toxicity.[24] Additionally, their synthesis routes are simple with less complex sensor fabrication and plant extracts, renewable biomass, and mild conditions, and reducing toxic waste. Moreover, green NPS can support additional roles such as degradation[25–28] and delivery.[29] Still, the main challenge of green NPs is the moderate sensitivity compared to the electrochemical sensors. However, their performance can be further enhanced by employing different electrode materials or surface modification strategies to improve sensitivity and selectivity toward atrazine.

In this work, *Bauhinia purpurea L.* is utilized for the first time as a green precursor to produce Cobalt oxide nanoparticles (Co–O NPs), which are further employed for the electrochemical sensing of atrazine (ATZ). We chose this biomass because multiple studies confirm that *Bauhinia purpurea L.* contains a wide spectrum of secondary metabolites and bioactive compounds such as flavonoids, triterpenes, tannins, steroids, glycoside, phenolics, fatty acids, saponins, carbohydrates, terpenoids amino acids, and lutine.[30–32] In sensor fabrication, naturally occurring functional moieties, such as alkaloids and flavonoids, play a key role in promoting efficient interactions with target molecules, accelerating charge transfer, and improving detection sensitivity.

The biosynthesized Co–O NPs, characterized by their eco-friendly nature, large active surface, and favorable electron-transport behavior, contributed to a remarkable enhancement in sensing performance, particularly in terms of sensitivity and selectivity toward ATZ. Overall, this research highlights the potential of green-synthesized Co–O NPs for advanced electrochemical applications and presents a comprehensive approach toward designing, constructing, and assessing an eco-conscious sensor capable of accurately monitoring ATZ concentrations.

2. Materials and methods

2.1. Chemical required

Cobalt nitrate hexahydrate (≥98%), sodium hydroxide (≥98%), hydrochloric acid (37%), potassium hydroxide (≥85%), Tris-HCl buffer (≥99%), graphite powder (≥99%), atrazine (≥98%), difenoconazole (≥98%), cypermethrin (≥98%), chlorimuron-ethyl (≥98%), imidacloprid (≥98%), tebuconazole (≥98%), and other chemicals were obtained from Sigma-Aldrich.

2.2. Green synthesis of cobalt nanoparticles (Co–O NPs)

Green synthesis of Co–O NPs was performed following the protocol of Din *et al.* (2024) with slight modifications.[33] To obtain the plant extract, 5 g of dried plant sample was immersed in 100 mL of deionized water and gently heated on a hot plate for about 45 min to facilitate the release of bioactive constituents. After heating, the mixture was filtered, and the clear filtrate was stored in a refrigerator. For the metal precursor, 1 M cobalt nitrate hexahydrate was made by dissolving 2.9103 g of the salt in 10 mL of deionized water. 20 mL of the prepared extract was combined with 10 mL of the cobalt nitrate solution, and the pH was carefully adjusted to 12 using NaOH. The reaction mixture was then heated and stirred at 75 °C for approximately 30 min. The resulting suspension was centrifuged at 8000 rpm for 20 min to separate the solid fraction. The obtained pellet was repeatedly washed, dried in a vacuum oven, and heated at 200 °C for 2 h before being ground into a fine powder. This powdered material was subsequently utilized for detailed physicochemical characterization.

2.3. Characterization of the synthesised Co–O NPs

The formation of Co–O NPs by bio-reduction of cobalt ions was characterized using various techniques. XRD, Raman, TGA, UV, PL, XPS, SEM-EDX & FTIR techniques were employed to study the structural and physicochemical properties of the synthesized material. To identify the surface functional groups, the produced nanoparticles and their composites were examined using a Bruker Tensor II, recording spectra between 400 and 4000 cm^{-1} at a scan rate of 10 kHz. The optical characteristics were evaluated using UV–Vis spectrophotometry across 200–800 nm. Crystallographic features of the prepared materials were determined through Bruker D8 XRD, with patterns collected in the 2θ range of approximately 5°–80° at a scanning rate of 6° min^{-1}. In addition, FESEM coupled with EDS (Zeiss ULTRA 55) was employed to visualize morphological features and assess elemental composition of the nanoparticles. Raman spectra were recorded using a 785 nm diode laser as the excitation source, and the scattered signal was gathered

through a 50× objective lens (STR-300, Seki Technotron Corp., Japan). A monochromator with 600 grooves per mm in combination with a Peltier-cooled CCD detector was employed for spectral acquisition. X-ray photoelectron spectroscopy (XPS) was used to evaluate the binding energies of the synthesized sample, with spectra recorded over an energy range of 10–1000 eV. The measurements were taken on a Thermo K-alpha system fitted with an aluminium source. Thermal stability was examined through thermogravimetric analysis (TGA) using a TA Instruments Q500 unit, with heating from 30 °C up to 800 °C at a constant rate of 10 °C per minute under a nitrogen environment. Photoluminescence (PL) measurements were carried out using a spectrofluorometer (FluoroMax +, Horiba Scientific).

2.4. Molecular docking studies

To elucidate the possible molecular-level interactions between the Co–O NPs and atrazine (ATZ), molecular docking simulations were performed. The three-dimensional structures of ATZ (PubChem CID: 2256) were obtained from the PubChem database in SDF format. The Co–O NPs nanoparticle crystal structure was obtained from the Crystallography Open Database. The optimized structures (from vesta software) were then converted into PDB format for subsequent docking analysis. In the docking protocol, Co–O NPs were designated as the receptor (macromolecule), while ATZ was treated as the ligand. The docking simulations were executed using AutoDock Tools (ADT) and AutoDock 4.2. A blind docking approach was adopted to allow the ligand to freely explore potential binding sites on the surface of Co–O NPs. The grid box dimensions were set to 88 × 40 × 40 points, with a grid spacing of 0.36 Å, to encompass the entire active surface of the receptor. The autogrid4 module was used to generate grid maps representing various interaction energies. Docking calculations were performed using the Lamarckian Genetic Algorithm (LGA), which combines a global genetic search with local optimization to efficiently sample conformational space. The parameters were set to a population size of 300 and 100 independent docking runs. All other parameters were maintained at their default values. Following docking, the generated conformations were ranked based on their predicted binding energy. The lowest-energy conformation (most favorable binding pose) was selected for detailed visualization and interaction analysis using Discovery Studio Visualizer (DSV).[34]

2.5. Electrochemical investigations

Electrochemical studies, including Cyclic Voltammetry (CV) and Differential Pulse Voltammetry (DPV), were performed on a CHI660D workstation (CH Instruments Inc., Austin, TX, USA). A conventional three-electrode arrangement was employed, consisting of a saturated calomel electrode as the reference electrode, a carbon paste electrode as the working electrode, and a platinum wire as the counter electrode. To fabricate the bare carbon paste electrode (BCPE), 0.243 g of powdered graphite was blended with 40 μL of silicone oil until a uniform consistency was achieved. The resulting paste was carefully packed into the electrode cavity, polished to a smooth surface, and then connected to the instrument using a copper lead. To prepare the modified carbon paste electrode (MCPE), 6 mg of the synthesized Co–O NPs was incorporated into 0.24 g of graphite powder along with 40 μL of silicone oil, and the mixture was processed as described for the BCPE. Reproducibility was verified by preparing a second MCPE using identical conditions. All voltammetric measurements were performed in a freshly prepared HCl buffer (0.1 M) containing ATZ, maintaining constant experimental parameters for both BCPE and MCPE. For a real sample evaluation, water samples were collected, filtered to remove particulate matter, and then spiked with atrazine to simulate contaminated environments. Analysis was conducted using the MCPE with the standard addition method to minimize matrix interference, and percentage recovery was calculated to evaluate accuracy within complex samples. Each electrochemical experiment was repeated three times to ensure reliability.[35]

3. Results and discussion

3.1. Characterization of the synthesized green Co–O NPs

FTIR. FTIR spectrum of Co–O NPs and the extract is shown in Fig. 1a. A broad absorption band around 3342 cm^{-1} is referred to as stretching vibrations of O–H from adsorbed water and/or moisture content on the nanoparticle surface.[36] The peak at 1627 cm^{-1} is attributed to C═O[37] and C–H of carboxylic acid, amide, or nitrate originating from plant extracts used in the synthesis or from precursor salts such as cobalt nitrate hexahydrate. Peaks at 1333 cm^{-1} with a shoulder at 1384 cm^{-1} have also been attributed to C–H or O–H stretching of moisture content.[38] Two bands of low intensities at 1045 and 826 cm^{-1} are assigned to C–O stretching, and CO_3^{2-} anions, respectively.[39,40] A peak at 906 cm^{-1} may refer to ═C–H stretch of aromatic rings developed from the plant extract.[41] Two sharp peaks at 543 and 654 cm^{-1} are assigned to the stretching vibrations of O–Co–O vibrations,[42] and Co–O stretching in tetrahedral coordination,[43] which confirms the successful development of Co–O NPs. Compared to the FTIR spectrum of *Bauhinia purpurea L.*, there are considerable decrease in the intensity of OH and C–H or C═O bonds in the FTIR spectrum of Co–O NPs. These correspond to capping by phytochemicals, especially alcohols, flavonoids, and phenolics.

TGA. The thermal behaviour of the nanoparticles is affected by the type of plant extract, precursor initial concentration, time, and temperature of calcination, and the solution's pH.[44,45] TGA analysis of Co–O NPs was conducted from room temperature to 900 °C (Fig. 1b). The analysis reveals three main weight loss steps; the first weight loss (%) begins from 43 °C up to 150 °C. This loss is attributed to the evaporation of absorbed water and moisture.[46] The second weight loss occurred in the range from 254 to 460 °C, due to the combustion and volatilization of organic species.[47] The major weight loss occurs in the 658–800 °C region, with an exothermic reaction detected in the derivative thermogravimetric (DTG) analysis during the third breakdown phase, highlighting temperature-dependent weight loss and exothermic processes. This weight loss may refer to the

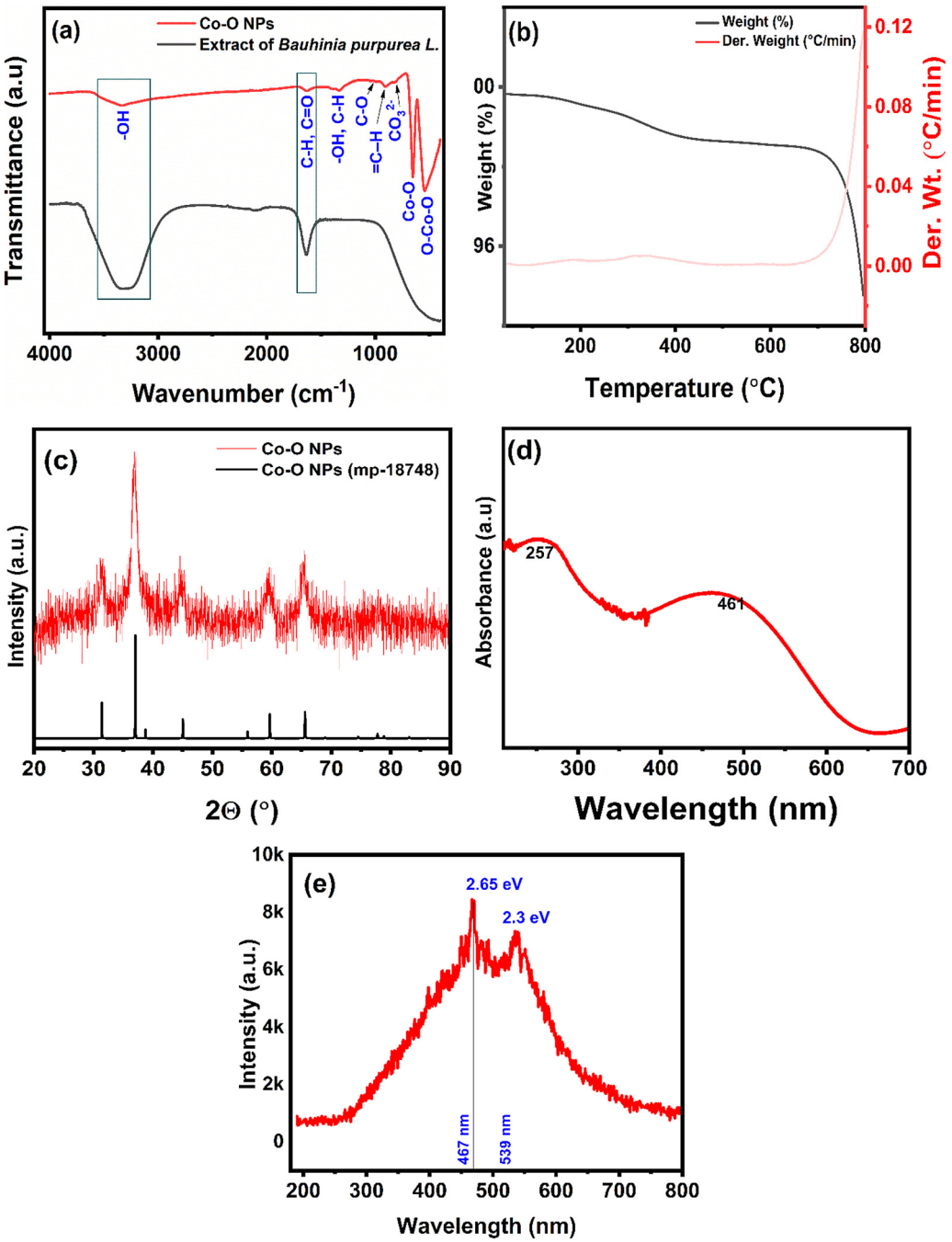

Fig. 1 (a) FT-IR spectrum of Co–O NPs, (b) TGA and DTG curves of Co–O NPs (c) XRD patterns of the as-synthesized Co–O NPs and the simulated one, (d) UV–VIS spectrum of Co–O NPs & (e) Photoluminescence spectrum of the Co–O NPs.

decomposition of Co_3O_4 to Co–O according to eqn (1). The overall weight loss of the developed Co–O NPs in this study, owing to the increment in temperature up to 800 °C, is only 5%. This indicates high thermal stability, favorable for electronic applications.

$$Co_3O_4 \rightarrow 3Co\text{–}O + \tfrac{1}{2}O_2 \quad (1)$$

XRD. The XRD pattern of Co–O NPs shows intense diffraction planes at (220), (311), (400), (511), (440) at $2\theta = 31.68$, 36.98, 44.2, 59.7, and 65.4, respectively (Fig. 1c). This typically matches standard Joint Committee on Powder Diffraction Standards (JCPDS) files, such as 74-2120 and 14-0673, confirming the cubic spinel structure of the developed Co–O NPs. The figure shows the XRD pattern of the developed Co–O NPs and the simulated one (mp-18748). The crystallite size of the developed Co–O NPs is calculated using Debye–Scherrer eqn (2).[48] The calculated crystallite size of Co–O NPs is 55.25 nm.

$$D = \frac{0.9\lambda}{\beta \cos\theta} \quad (2)$$

where θ, β, λ, and D are the Bragg's angle, full width at half maximum, X-ray wavelength, and crystallite size, respectively.

UV. In the UV–VIS spectrum of Co–O NPs (Fig. 1d), there are two broad peaks around 260 nm and 461 nm. These peaks refer to the charge transfer from O^{2-} ligand to Co^{2+} and Co^{3+} metal ions, respectively.[49,50] This suggests the presence of Co–O and Co_3O_4. These peaks arise from the continuous fluctuation of thelectrons in the conduction band of the nanoparticles generated *via* the binding of an electromagnetic field.[51] However, the plasmon absorption in Co–O NPs is dependent on the route of synthesis, particle size, surface adsorbed species, and dielectric medium.[52]

PL. The optical characteristics of nanomaterials are strongly related to their morphologies and nanostructures. Fig. 1e presents the photoluminescence (PL) spectrum of the Co–O NPs. The PL spectrum shows broad peaks in the visible region, indicative of deep-level emission. These peaks refer to the structural defects and impurities in the crystal, for instance, cobalt interstitials and oxygen vacancies,[53] in addition to charge-compensating defects. The peak around 539 nm (2.3 eV) corresponds to near-band-edge emission, also known as excitonic emission between the valence and conduction bands. However, this peak is slightly shifted from its original value (2.0–2.2 eV) due to quantum confinement effects in nanostructures.[54] The second emission peak at 467 nm (2.65 eV) arises due to the radiative transitions originating from the crystalline defects in Co_3O_4 NPs. Also, it could be related to the ligand field charge transfer between Co^{2+} and Co^{3+} ions and between oxygen and Co ions.[55] The energy value of each peak has been calculated using the equation: E_g (eV) = $1240/\lambda_{em}$ (nm).[56]

XPS. The XPS full spectrum of Co–O NPs confirms the presence of Co, O (Fig. 2a). The high-resolution XPS spectrum of the Co 2p region (Fig. 2b) shows two main spin–orbit components of Co $2p_{3/2}$ and Co $2p_{1/2}$ at with two strong peaks at 779.78 eV and 795.55 eV, in addition to two satellite peaks at 781.25 and 802.18 eV. This indicates the presence of Co^{2+} species (specifically Co(II) oxide CoO).[57] The spin energy separation (ΔE) between these peaks is a key indicator of the cobalt phase: a ΔE of 16.0 eV is characteristic of the CoO spinel phase, while a ΔE of 15.0 eV suggests Co_3O_4. In this study, XPS reveals ΔE = 15.77 eV. This is referred to that there is a partial reduction of Co^{3+} to Co^{2+}, suggesting the presence of both Co^{2+} and Co^{3+} species with generating oxygen vacancies,[58] indicating the coexistence of these oxidation states within the nanoparticles and the efficiency of the developed Co–O NPs for electrochemical detection. The high resolution XPS of O 1s is shown in Fig. 2c. The deconvolution of the peak shows three

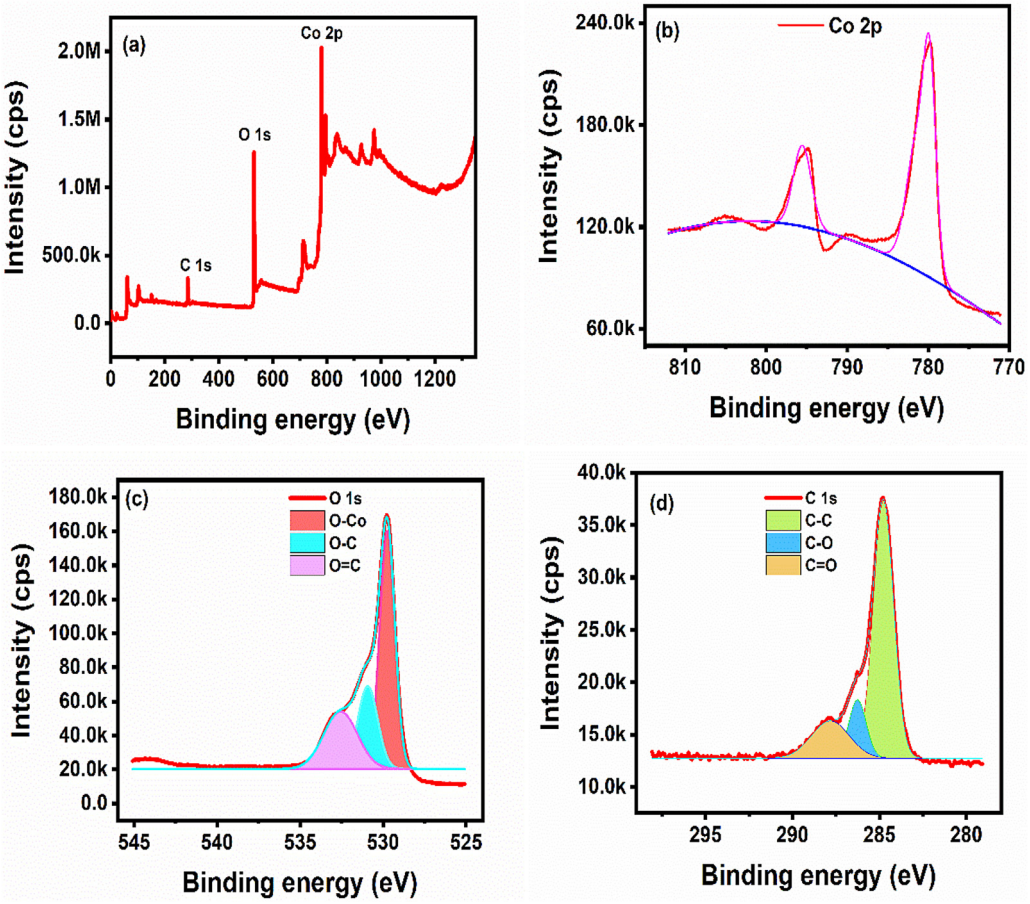

Fig. 2 XPS spectrum (full survey) of Co–O NPs (a), and high-resolution XPS spectra of Co 2p (b), O 1s (c) and C 1s (d).

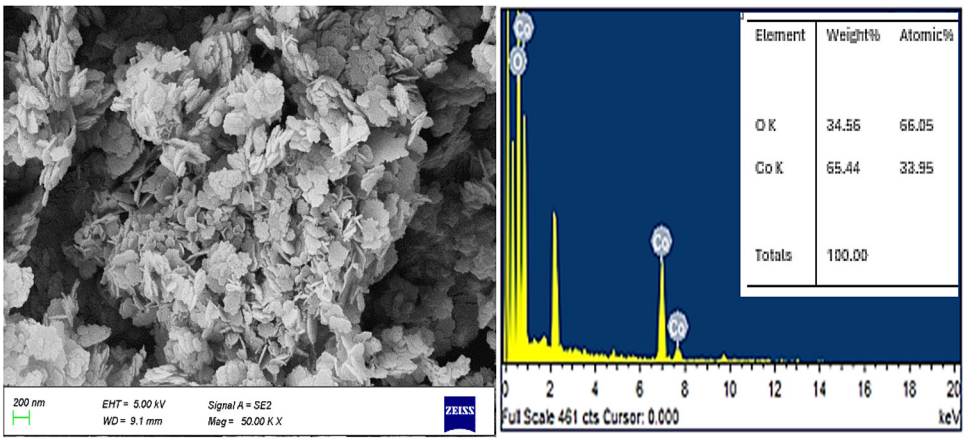

Fig. 3 SEM image and EDS results of Co–O NPs.

peaks located at 529.74, 530.92, 532.56 eV ascribed to O–Co, O–C and O═C bonding, respectively.[58] The C1s peak was deconvoluted into three different component peaks at 284.78, 286.26 eV, and 287.81 eV (Fig. 3d), representing C–C, C–O, and C═O.[59]

SEM. The surface morphology of the as-synthesized Co–O NPs was examined by SEM-EDS. The SEM image (Fig. 3) shows that Co–O NPs have a thin plate-like morphology. The fragmented platelets are irregularly shaped, close to circular, and slightly aggregated. The observed agglomeration is common in bio-synthesized nanoparticles, and this agglomeration is dependent upon the plant extract and the bio-compounds that are present in this extract. These bio-compounds have specific surface functional groups like amine, hydroxyl, and carboxylic, which are responsible for passivating the Co–O NPs surface. Also, these functional groups may contribute to the intermolecular hydrogen bonding that led to the agglomeration of Co–O NPs.[60] The sizes of the platelets are mainly in the range of 50–300 nm. Moreover, the thickness of the different platelets is uniform. Suggesting a high surface area available for electrochemical applications. EDS consistently confirms the presence of cobalt (65.44 wt%) and oxygen (34.56 wt%) as the main elements in cobalt oxide nanoparticles (Fig. 3), verifying the purity and oxide structure of the developed Co–O NPs

3.2. Docking results

The top-ranked docking pose revealed a binding energy of −1.15 kcal mol^{-1}, and an estimated inhibition constant (K_i) of 144.40 mM at 298 K. The electrostatic component of the binding energy was −2.34 kcal mol^{-1}, suggesting that non-electrostatic forces, such as hydrogen bonding, van der Waals interactions, and hydrophobic effects, dominate the complex's stabilization. There are two hydrogen bonds between Co–O NPs and ATZ, having distances of 2 and 1.9 angstroms (Fig. 4). The negative binding energy indicates a spontaneous and thermodynamically favorable interaction between ATZ and the Co–O NPs surface.[61,62]

3.3. Electrochemical characterization of cobalt oxide NPs/CPE

The electrocatalytic activity of the fabricated sensor was investigated by cyclic voltammetry at the Co–O NPs/CPE and

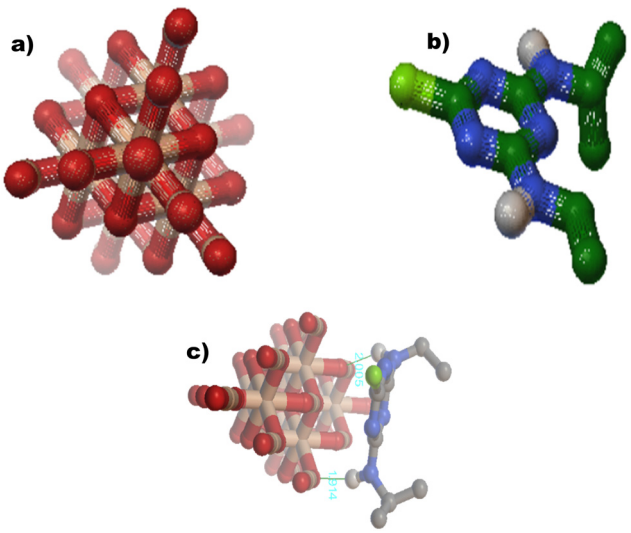

Fig. 4 3D structure of (a) Co–O NPs, (b) Atrazine, (c) Top-ranked docked conformation of Co–O NPs and atrazine complex as visualized using AutoDock, showing the hydrogen bonds.

compared with that of the bare carbon paste electrode. The CV responses were recorded in a 0.01 M KCl buffer containing 1 mM ferricyanide, within the potential window of −0.5 to +0.6 V at a scan rate of 50 mV s^{-1}. As depicted in Fig. 5a, the bare CPE exhibited a low current, indicating sluggish electron-transfer kinetics. In contrast, the Co–O NPs/CPE showed a well-defined pair of redox peaks with enhanced peak currents, confirming the excellent electrocatalytic activity of the Co–O NPs modifier. Further, the effect of Co–O NPs modifier on ATZ detection was investigated using the CV technique in a 0.1 M HCl buffer containing 20 mM of ATZ. From Fig. 5b, a pronounced increase in current with distinct redox features at 0.2 V and 0.3 V is observed, confirming the enhanced electrocatalytic activity of the Co–O NPs modifier toward ATZ detection.

3.3.1. Effect of buffer. The effect of supporting electrolyte on the voltammetric behavior of ATZ at the MCPE was

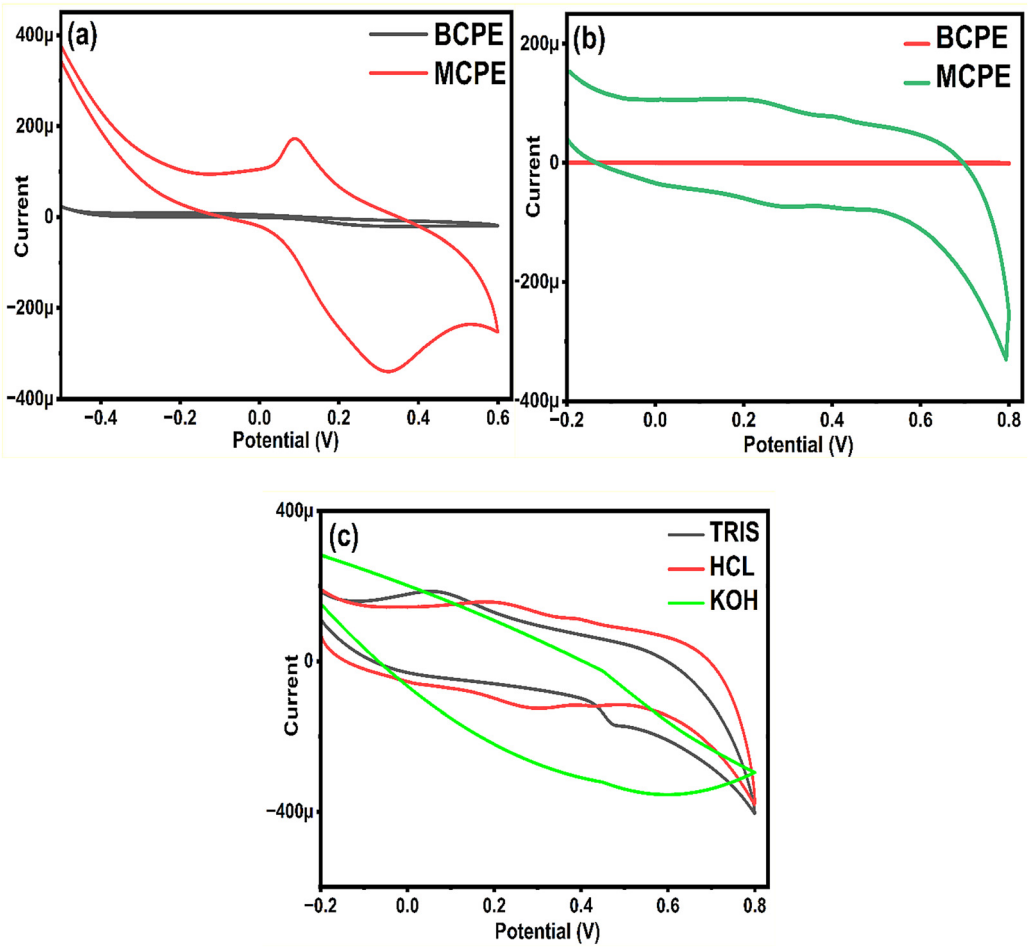

Fig. 5 (a) Electrochemical characterization of Co–O NPs/CPE using Potassium ferricyanide in KOH buffer, (b) effect of Co–O NPs/CPE on ATZ in HCl buffer, (c) effect of buffer on Co–O NPs/CPE towards ATZ.

examined using 0.1 M KOH, 0.1 M Tris buffer, and 0.1 M HCl in the presence of 20 mM ATZ. The recorded voltammograms (Fig. 5c) indicate that the electrochemical response is strongly influenced by the electrolytic medium. KOH produced the highest current intensity, reflecting enhanced conductivity and faster charge-transfer processes in alkaline conditions. However, the peaks obtained in KOH were relatively broad. In contrast, HCl exhibited more well-defined and sharper redox peaks, suggesting better peak resolution and a more stable electrochemical transformation of atrazine in an acidic medium. The response in the Tris buffer was intermediate between the two. These results demonstrate that while KOH favors higher sensitivity, HCl provides superior peak definition, highlighting the significant role of buffer environment in the electrochemical behavior of ATZ. Therefore, HCl was used for further experiments.

3.3.2. Effect of Scan rate. The influence of scan rate on the voltammetric response of ATZ at the Co–O NPs/CPE electrode was investigated to elucidate the electrode reaction kinetics. Fig. 6a presents the cyclic voltammograms recorded in the presence of 20 mM ATZ over a scan rate (ν) range of 10–60 mV s^{-1}. The results show that the redox peak currents (I_p) increase progressively with increasing scan rate, indicating enhanced electron-transfer activity at higher potential sweep rates. The plot of log I_p *versus* log ν yielded a slope of approximately 0.8, suggesting that the redox reaction of atrazine at Co–O NPs/CPE is governed by a mixed diffusion–adsorption-controlled mechanism rather than a purely surface-confined or diffusion-controlled process (Fig. 6b). This behavior indicates that both mass transport from the bulk solution and partial adsorption of ATZ on the modified electrode surface contribute to the overall electrochemical response.[63]

3.3.3. Effect of concentration variation. The concentration-dependent electrochemical behavior of ATZ at the Co–O NPs/CPE electrode was examined in the range of 20–200 μM. The cyclic voltammograms demonstrated a gradual, systematic increase in the cathodic peak current with increasing ATZ concentration (Fig. 6c), indicating efficient accumulation and electron transfer of ATZ at the modified electrode surface. Along with the current enhancement, a slight positive shift in peak potential was observed at higher concentrations, indicating minor changes in interfacial kinetics and possible adsorption of ATZ on the Co–O NPs-modified matrix.

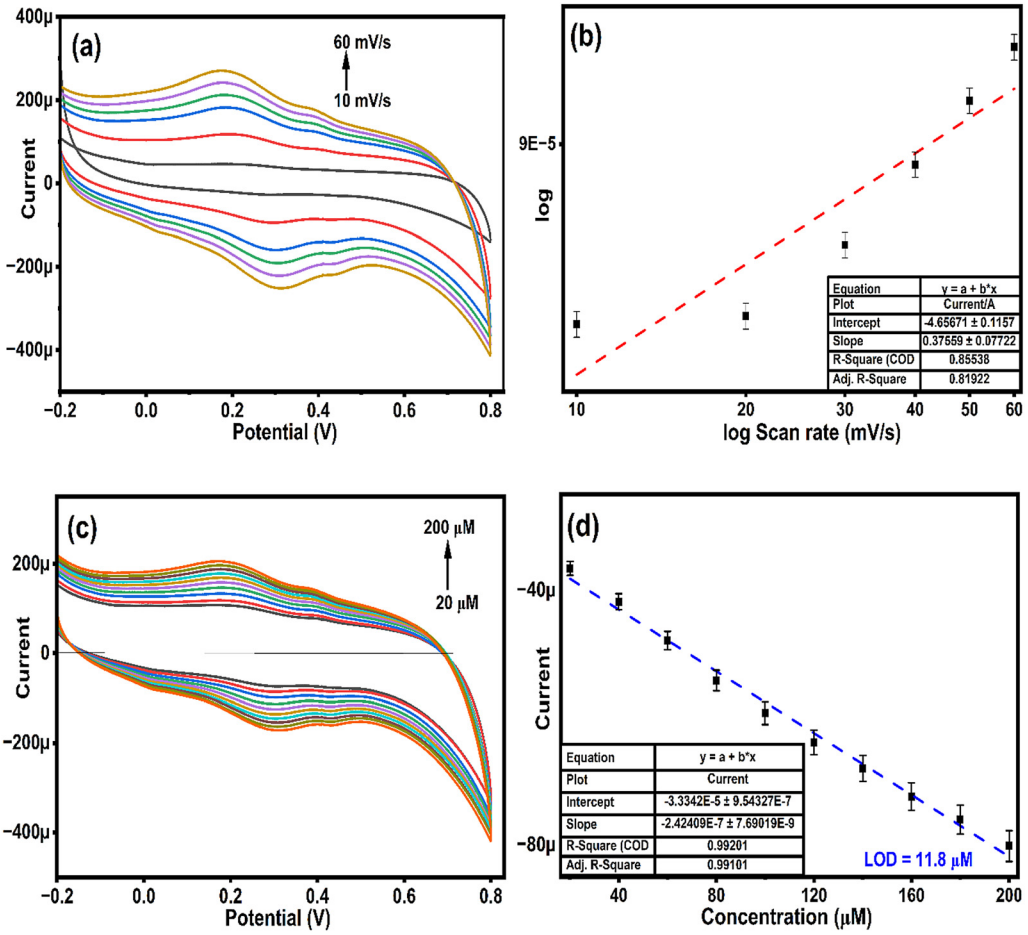

Fig. 6 (a) Effect of scan rate of Co–O NPs/CPE, (b) Log scan rate *vs.* Log current of Co–O NPs/CPE in presence of ATZ, (c) effect of Concentration variation of ATZ on Co–O NPs/CPE, (d) Concentration *vs.* current linear plot.

The calibration plot constructed from cathodic peak currents showed excellent linearity and followed the regression equation: I_p (A) = -2.42×10^{-7} C $- 3.33 \times 10^{-5}$ (R^2 = 0.992), confirming the proportional relationship between concentration and oxidation response. Using the signal-to-noise method (3σ/m), the limit of detection (LOD) was determined to be 11.8 µM (Fig. 6d), highlighting the sensor's good sensitivity. The stable peak shape and reproducible current increment across the studied range further validate the reliability of the Co–O NPs/CPE electrode for quantitative analysis.

The formation of Co nanoparticles involves the reduction of Co^{2+} to metallic Co^0. Upon exposure to aqueous and ambient conditions, the nanoparticle surface is partially oxidized to form $Co(OH)_2$/CoOOH species. During electrochemical measurements, a reversible Co^{2+}/Co^{3+} redox transition occurs ($Co(OH)_2 + OH^- \leftrightarrow CoOOH + H_2O + e^-$), which plays a key role in electron transfer. Atrazine (ATZ) is adsorbed onto the Co NP surface and undergoes oxidation, contributing to the observed current response. This process leads to an enhanced electrochemical signal, forming the basis of ATZ detection.

Table 1 reveals linear range and LOD of Co–O NPs/CPE compared to that reported in literature. These findings demonstrate that the Co–O NPs/CPE platform provides effective electrocatalytic activity and a wide linear working range, making it a promising candidate for the practical electrochemical determination of ATZ.

3.3.4. Repeatability and stability. The effectiveness of the Co–O NPs/CPE as an electrochemical sensor was evaluated through studies on repeatability and stability. To assess repeatability, six Co–O NPs/CPEs were independently fabricated using the same preparation procedure, and their electrochemical responses toward 10 µM atrazine were recorded in a freshly prepared buffer solution. The results (Fig. 7a) showed a relative standard deviation (RSD) of 6.7% for the oxidation peak current, demonstrating excellent reproducibility of the electrode fabrication and reliable analytical performance. Further control experiments and reproducibility studies were not included in the present work and are recommended for future studies to further validate the method's reliability.

The stability of the Co–O NPs/CPE was further examined by cyclic voltammetry over 50 successive cycles in the potential window of −0.2 to 0.6 V. After the 50th cycle, only an ≈10% decrease in the oxidation peak current of ATZ was observed compared with the initial cycle (Fig. 7b), confirming the strong

Table 1 A comparison of the efficiencies of different electrodes compared to Co–O NPs/CPE in terms of linear range and LOD

Electrode	Linear range (μM)	Limit of detection (μM)	Ref.
Electro-spun SnO_2 nanofiber	0.01–1	0.09	64
Tyrosinase immobilization on polyvinyl alcohol with styryl-pyridinium groups	10–100	1.3	65
GNPs	0.21–2.1	0.016	66
SiO_2@atrazine-MIP nanoparticles	—	1.8	67
Ha006a/MCPE	10–100	5.4	
Boron-doped diamond electrode	0.05–40	0.01	68
Cell-free sensor	—	20	69
MIP-based screen-printed potentiometric cell	0.5–5	0.4	70
Molecularly imprinted conducting polymer	0.001–15000	0.4	71
ZnO NPs	0.5–3	1.9	72
Co–O NPs/CPE	20 to 200	11.8	Present work

stability and resistance to surface fouling of the modified electrode. These findings indicate that the Co–O NPs/CPE possess good durability and are suitable for repeated measurements without significant loss of activity.

3.3.5. Effect of interferences. The selectivity of the Co–O NPs/CPE sensor toward ATZ was evaluated in the presence of commonly coexisting pesticide molecules, including chlorpyrifos (Chlorin), cypermethrin (Cyper), difenoconazole (Difen), imidacloprid (Imi), and tebuconazole (Tebu). As shown in Fig. 7c, the individual interferents produced comparatively low cathodic peak currents, whereas the addition of atrazine to each system resulted in a significant increase in current response. The distinct enhancement in peak current for the mixtures containing interferent + ATZ confirms that the sensor response is predominantly governed by ATZ rather than the coexisting species. These results clearly demonstrate that the Co–O NPs/CPE exhibit high selectivity toward ATZ, even in the presence of structurally similar pesticides, highlighting their

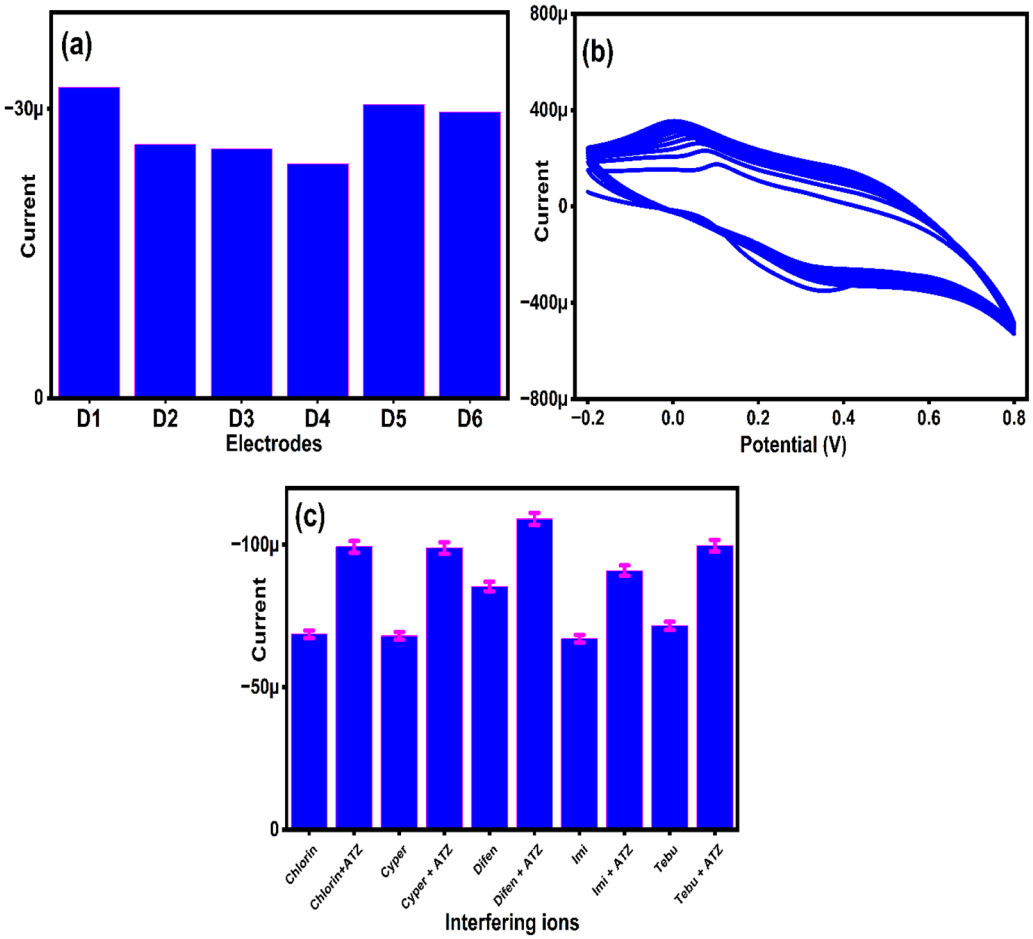

Fig. 7 (a) Repeatability of Co–O NPs/CPE, (b) stability of Co–O NPs/CPE, and (c) effect of interference molecules on Co–O NPs/CPE in the presence of ATZ.

Table 2 Percentage of recoveries of Co–O NPs/CPE in different water matrices

Sample type	Added concentration (μM)	Obtained concentration (n = 3) (μM)	Recovery percentage (%)
Distilled water	6	5.94 ± 0.04	99.00
	12	11.87 ± 0.09	98.92
	18	17.43 ± 0.08	96.83
Tap water	6	5.81 ± 0.07	96.83
	12	11.58 ± 0.13	96.50
	18	16.94 ± 0.11	94.11
STP water	6	5.22 ± 0.06	87.00
	12	10.98 ± 0.23	91.50
	18	15.54 ± 0.45	86.33

suitability for real-sample analysis where multiple contaminants may coexist.

3.3.6. Real sample analysis. The Co–O NPs/CPE sensor was used for the detection of ATZ in distilled water, tap water, and STP water. Samples were centrifuged at 8000 rpm for 10 min to remove suspended matter, and the supernatant was spiked with known atrazine concentrations for tap water and wastewater samples (Table 2). Atrazine levels were quantified using peak current responses and a linear calibration equation. Higher recovery percentage was obtained in distilled water than in tap water, while a slight reduction in wastewater was attributed to matrix interferences. Nevertheless, the sensor demonstrated reliable performance in wastewater, confirming its suitability for real-sample analysis.

Conclusion

The present work reports the green synthesis of Co–O NPs nanoparticles using *Bauhinia purpurea L.* leaf extract as an eco-friendly reducing agent. Structural and physicochemical characterization confirmed the successful formation of crystalline nanoparticles with suitable surface functionality for sensing applications. Molecular docking studies indicated favorable interactions between Co–O NPs nanoparticles and atrazine, supporting their affinity toward the target analyte. The fabricated electrochemical sensor exhibited a linear detection range of 20–200 μM with a detection limit of 11.8 μM. Recovery values of 86.33 to 99% in distilled, tap and STP water samples demonstrated good accuracy and practical applicability. The study establishes a sustainable platform for atrazine monitoring in environmental water systems.

Conflicts of interest

There are no conflicts to declare.

Data availability

The datasets generated and/or analyzed during the current study are available from the corresponding author upon reasonable request. All relevant experimental data, including adsorption experiments, characterization results, and molecular docking outputs, have been thoroughly documented and can be provided to support the findings of this research.

Acknowledgements

Dr Simranjeet Singh would like to acknowledge the DBT HRD Project & Management Unit, Regional Center for Biotechnology, NCR Biotech Science Cluster, Faridabad, Haryana, for the Research Associateship (DBT-RA), fellowship under the award letter no. DBT-RA/2022/July/no./2044 dated January 12, 2023. The authors wish to express their gratitude to the Ministry of Education (MoE) for their fellowship support under the grant MoE-STARS/STARS-2/2023-0714, dated September 26, 2022. Radhika Varshney would like to acknowledge the MoE, Government of India, for the Prime Minister's Research Fellowship (PMRF): TF/PMRF-22-5459.

References

1 R. C. Gupta and P. K. Gupta, *Vet. Toxicol.*, 2025, 565–579.
2 R. Mohd Ghazi, N. R. Nik Yusoff, N. S. Abdul Halim, I. R. A. Wahab, N. Ab Latif, S. H. Hasmoni, M. A. Ahmad Zaini and Z. A. Zakaria, *Bioengineered*, 2023, **14**, 2259526.
3 N. Sathiakumar, P. A. MacLennan, J. Mandel and E. Delzell, *Crit. Rev. Toxicol.*, 2011, **41**, 1–34.
4 M. Mela, I. C. Guiloski, H. B. Doria, M. A. F. Randi, C. A. de Oliveira Ribeiro, L. Pereira, A. C. Maraschi, V. Prodocimo, C. A. Freire and H. C. Silva de Assis, *Ecotoxicol. Environ. Saf.*, 2013, **93**, 13–21.
5 A. Sharma, A. Shukla, K. Attri, M. Kumar, P. Kumar, A. Suttee, G. Singh, R. P. Barnwal and N. Singla, *Ecotoxicol. Environ. Saf.*, 2020, **201**, 110812.
6 J. Ma, S. Wang, P. Wang, L. Ma, X. Chen and R. Xu, *Ecotoxicol. Environ. Saf.*, 2006, **63**, 456–462.
7 H. He, Y. Liu, S. You, J. Liu, H. Xiao and Z. Tu, *Int. J. Environ. Res. Public Health*, 2019, **16**, 5129.
8 N. F. Abd Rani, K. Ahmad Kamil, F. Aris, N. Mohamed Yunus and N. A. Zakaria, *Biocatal. Biotransform.*, 2022, **40**, 233–247.
9 S. Singh, V. Kumar, D. S. Dhanjal, V. Dhaka, Sonali and J. Singh, *Agricultural Biocatalysis: Theoretical Studies and Photosynthesis Aspects*, Pan Stanford Publishing Pte. Ltd, 2022, pp. 295–312.
10 H. Zhao, H. Qian, J. Cui, Z. Ge, J. Shi, Y. Huo, Y. Zhang and L. Ye, *Toxicology*, 2024, **505**, 153846.
11 A. N. Kabra, M.-K. Ji, J. Choi, J. R. Kim, S. P. Govindwar and B.-H. Jeon, *Environ. Sci. Pollut. Res.*, 2014, **21**, 12270–12278.
12 K. Ralston-Hooper, J. Hardy, L. Hahn, H. Ochoa-Acuña, L. S. Lee, R. Mollenhauer and M. S. Sepúlveda, *Ecotoxicology*, 2009, **18**, 899–905.
13 C. Steffens, S. C. Ballen, E. Scapin, D. M. da Silva, J. Steffens and R. A. Jacques, *Sens. Actuators Rep.*, 2022, **4**, 100096.
14 S. Singh, N. A. Khan, R. Ramadan, N. Shehata, D. Kapoor, D. S. Dhanjal, N. Sivaram, J. Singh, D. Barceló and

P. C. Ramamurthy, *Desalination Water Treat.*, 2024, **317**, 100201.
15 X. Liu, W. J. Li, L. Li, Y. Yang, L. G. Mao and Z. Peng, *Sens. Actuators, B*, 2014, **191**, 408–414.
16 M. Yang, X. Zhao, S. Zheng, X. Liu, B. Jin, H. Li and Y. Gan, *J. Electroanal. Chem.*, 2017, **791**, 17–22.
17 L. Fan, C. Zhang, W. Yan, Y. Guo, S. Shuang, C. Dong and Y. Bi, *Talanta*, 2019, **201**, 156–164.
18 R. Manikandan, J. Park, H. G. Jang, U. A. Mugunthan, C. S. Kim, B. S. Shin, J. H. Yoon and S. C. Chang, *J. Environ. Chem. Eng.*, 2026, **14**, 120667.
19 S. Singh, N. Pavithra, H. Kaur, R. Varshney, N. A. Khan, R. Kumar, A. K. Sharma, J. Singh and P. C. Ramamurthy, *Sci. Rep.*, 2024, **14**, 17662.
20 M. L. Yola and N. Atar, *Ind. Eng. Chem. Res.*, 2017, **56**, 7631–7639.
21 P. Supraja, V. Singh, S. R. K. Vanjari and S. Govind Singh, *Microsyst. Nanoeng.*, 2020, **6**, 3.
22 C. Zhang, S. Si and Z. Yang, *Sens. Actuators, B*, 2015, **211**, 206–212.
23 J. C. K. Spiro, K. K. Mishra, V. N. Dhamu, A. Bhatia, S. Muthukumar and S. Prasad, *Sens. Diagn.*, 2024, **3**, 1835–1842.
24 S. S. Raut, A. Sharma, R. Yadav, S. Kumar, A. Shukla, A. Singh and A. Mishra, *J. Environ. Chem. Eng.*, 2026, **14**, 121102.
25 H. Chemingui, R. Lafi, T. Missaoui, I. Montasser, A. Hafiane and M. Kamoun, *BioCB*, 2025, **15**, 4281–4299.
26 H. Chemingui, T. Missaoui, J. C. Mzali, T. Yildiz, M. Konyar, M. Smiri, N. Saidi, A. Hafiane and H. C. Yatmaz, *Mater. Res. Exp.*, 2019, **6**, 1050b4.
27 H. Chemingui, A. Moulahi, T. Missaoui, A. H. Al-Marri and A. Hafiane, *Environ. Technol.*, 2024, **45**, 926–944.
28 H. Chemingui, M. Kahloul, B. El Abed, T. Ben Amor and A. Hafiane, *Clean Technol. Environ. Policy*, 2024, **26**, 3273–3295.
29 K. R. Pooja, G. Nagaraju, C. P. Prajwal Ujjani, V. J. Koti, K. B. Naveen, R. Harini, J. Manjanna and C. Mallikarjunaswamy, *J. Cluster Sci.*, 2025, **36**, 133.
30 B. S. Negi, B. P. Dave and Y. K. Agarwal, *Indian J. Microbiol.*, 2012, **52**, 360–365.
31 Z. A. Zakaria, L. Y. Wen, N. I. Abdul Rahman, A. H. Abdul Ayub, M. R. Sulaiman and H. K. Gopalan, *Med. Princ. Pract.*, 2007, **16**, 443–449.
32 Z. A. Zakaria, E. E. Abdul Hisam, M. S. Rofiee, M. Norhafizah, M. N. Somchit, L. K. Teh and M. Z. Salleh, *J. Ethnopharmacol.*, 2011, **137**, 1047–1054.
33 M. I. Din, Z. Hussain, N. Siddique, A. Sharif, A. Intisar, E. Ahmed and M. Arshad, *Desalination Water Treat.*, 2024, **317**, 100100.
34 S. Singh, N. Pavithra, R. Varshney, A. Panchal, N. Shehata, N. A. Khan, J. Singh and P. C. Ramamurthy, *Nanoscale Adv.*, 2025, **7**, 7273–7284.
35 P. Narasimhappa, R. Varshney, S. Singh, T. S. Kumar Naik and P. C. Ramamurthy, *Chemosphere*, 2023, **333**, 138977.
36 M. Safaei, M. Taran, L. Jamshidy, M. M. Imani, H. R. Mozaffari, R. Sharifi, A. Golshah and H. Moradpoor, *Int. J. Biol. Macromol.*, 2020, **158**, 477–485.
37 M. Hafeez, R. Shaheen, B. Akram, A. Zain-Ul-, S. Haq, S. Mahsud, S. Ali and R. T. Khan, *Mater. Res. Express*, 2020, **7**, 025019.
38 A. Sajid, M. Amjad, Q. Manzoor, S. Wazir, A. Sajid, N. Alwadai, M. Iqbal and N. Tamam, *Int. J. Biol. Macromol.*, 2024, **274**, 133194.
39 D. A. Kader, *Mater. Today Sustain.*, 2024, **28**, 100997.
40 A. K. Worku, A. Asfaw and D. W. Ayele, *Front. Chem.*, 2024, **12**, 1357127.
41 R. D. Kale and P. B. Kane, *Groundw. Sustain. Dev.*, 2019, **8**, 309–318.
42 S. Iravani and R. S. Varma, *Green Chem.*, 2020, **22**, 2643–2661.
43 S. Shahabuddin, N. M. Sarih, F. H. Ismail, M. M. Shahid and N. M. Huang, *RSC Adv.*, 2015, **5**, 83857–83867.
44 M. Zaib, A. Nazir, T. Shahzadi, T. Riaz, U. Z. Ijaz, U. Farooq, A. Khalid, P. Ahmad and M. Hasan, *Inorg. Chem. Commun.*, 2026, **183**, 115654.
45 H. A. Hassanin, A. Taha and E. Afkar, *Ceram. Int.*, 2021, **47**, 3099–3107.
46 J. G. Suma, M. B. Megalamani, Y. N. Patil, S. D. Kotabagi, S. R. Kurundawade, S. K. Rajappa and S. T. Nandibewoor, *Mater. Sci. Eng., B*, 2026, **323**, 118884.
47 C. O. Chikere, E. Hobben, N. H. Faisal, P. Kong-Thoo-Lin and C. Fernandez, *Microchem. J.*, 2021, **160**, 105668.
48 N. Chokkiveettil, D. K. Unnikrishnan, D. J. Priya, D. Chandran, S. Gopalsamy and R. Rajamani, *Microchem. J.*, 2026, **220**, 116325.
49 Z. Nate, A. A. S. Gill, R. Chauhan and R. Karpoormath, *Microchem. J.*, 2021, **160**, 105709.
50 T. O. Ahmadov, Z. Durmus, A. Baykal and H. Kavas, *Inorg. Mater.*, 2011, **47**, 426–430.
51 U. Kreibig and M. Vollmer, *Optical properties of metal clusters*, Springer Science & Business Media, 2013, **25**.
52 I. Lisiecki and M. P. Pileni, *Langmuir*, 2003, **19**, 9486–9489.
53 R. Al-Tuwirqi, A. A. Al-Ghamdi, N. A. Aal, A. Umar and W. E. Mahmoud, *Superlattices Microstruct.*, 2011, **49**, 416–421.
54 C. Ravi Dhas, R. Venkatesh, D. David Kirubakaran, J. Princy Merlin, B. Subramanian and A. Moses Ezhil Raj, *Mater. Chem. Phys.*, 2017, **186**, 561–573.
55 A. Llavona, C. Díaz-Guerra, M. C. Sánchez and L. Perez, *Mater. Chem. Phys.*, 2010, **124**, 1177–1181.
56 L. Zhu, Y. Zheng, T. Hao, X. Shi, Y. Chen and J. Ou-Yang, *Mater. Lett.*, 2009, **63**, 2405–2408.
57 H. Singh, A. K. Sinha, M. N. Singh, P. Tiwari, D. M. Phase and S. K. Deb, *J. Phys. Chem. Solids*, 2014, **75**, 397–402.
58 R. Kumar, A. Soam and V. Sahajwalla, *Mater. Adv.*, 2021, **2**, 2918–2923.
59 X. Tang, Q. Feng, J. Huang, K. Liu, X. Luo and Q. Peng, *J. Colloid Interface Sci.*, 2018, **510**, 368–375.
60 N. A. Dhas, C. P. Raj and A. Gedanken, *Chem. Mater.*, 1998, **10**, 1446–1452.

61 A. Naifar, K. Oueslati, F. Aouaini, B. Basha and A. Ben Lamine, *Langmuir*, 2025, **41**, 12781–12791.
62 Y. L. Salomón, J. Georgin, D. G. P. Allasia, M. S. Netto, C. O. Aniagor, J. O. Ighalo and D. S. P. Franco, *Sustainability*, 2025, **17**, 10455.
63 S. Singh, P. N, R. Varshney, A. Panchal, P. C. Ramamurthy, J. Singh and N. Shehata, *Sci. Rep.*, 2025, **15**, 45024.
64 P. Supraja, S. Tripathy, S. R. Krishna Vanjari, V. Singh and S. G. Singh, *Biosens. Bioelectron.*, 2019, **141**, 111441.
65 C. Tortolini, P. Bollella, R. Antiochia, G. Favero and F. Mazzei, *Sens. Actuators, B*, 2016, **224**, 552–558.
66 X. Liu, W. J. Li, L. Li, Y. Yang, L. G. Mao and Z. Peng, *Sens. Actuators, B*, 2014, **191**, 408–414.
67 R. Liu, G. Guan, S. Wang and Z. Zhang, *Analyst*, 2010, **136**, 184–190.
68 Ľ. Švorc, M. Rievaj and D. Bustin, *Sens. Actuators, B*, 2013, **181**, 294–300.
69 A. D. Silverman, U. Akova, K. K. Alam, M. C. Jewett and J. B. Lucks, *ACS Synth. Biol.*, 2020, **9**, 671–677.
70 G. Alberti, C. Zanoni, S. Spina, L. R. Magnaghi and R. Biesuz, *Chemosensors*, 2022, **10**, 339.
71 B. Liu, J. Yan, M. Wang and X. Wu, *Int. J. Electrochem. Sci.*, 2019, **14**, 3610–3617.
72 S. Singh, N. Pavithra, R. Varshney, A. Panchal, N. Shehata, N. A. Khan, J. Singh and P. C. Ramamurthy, *Nanoscale Adv.*, 2025, **7**, 7273–7284.